New X-Ray Microtomography Setups and Optimal Scan Conditions to Investigate Methane Hydrate-Bearing Sand Microstructure

Thi Xiu Le, Patrick Aimedieu, Michel Bornert, Baptiste Chabot, Andrew King, Anh Minh A.M. Tang

New X-ray microtomography setups and optimal scan conditions to investigate methane hydrate-bearing sand microstructure

*Thi Xiu Le, Patrick Aimedieu, Michel Bornert, Baptiste Chabot, Andrew King, Anh Minh Tang**

Laboratoire Navier, Ecole des Ponts ParisTech, CNRS UMR 8205, Univ. Gustave Eiffel, Marne-la-Vallée, France

**Corresponding authors:*

Dr. Anh Minh Tang
6-8 avenue Blaise Pascal, 77455 Champs-sur-Marne, France
anh-minh.tang@enpc.fr
Dr. Thi Xiu Le
6-8 avenue Blaise Pascal, 77455 Champs-sur-Marne, France
thi-xiu.le@enpc.fr
Dr. Patrick Aimedieu
6-8 avenue Blaise Pascal, 77455 Champs-sur-Marne, France
patrick.aimedieu@enpc.fr
Dr. *Michel Bornert*
6-8 avenue Blaise Pascal, 77455 Champs-sur-Marne, France
michel.bornert@enpc.fr
Baptiste Chabot
6-8 avenue Blaise Pascal, 77455 Champs-sur-Marne, France
Baptiste.Chabot@enpc.fr
Dr. Andrew King
Synchrotron Soleil, D306, Route de Belle Image, l'Orme des Merisiers, 91190 Saint-Aubin, France
king@synchrotron-soleil.fr

Abstract

Methane hydrates, naturally formed at high pressure and low temperature in marine and permafrost sediments, represent a great potential energy resource but also a considerable geo-hazard and climate change source. Investigating the grain-scale morphology of methane hydrate-bearing sandy sediments is crucial for the interpretation of geophysical data and reservoir-scale simulations in the scope of methane gas production as methane hydrate morphologies and distribution within the porous space significantly impact their macroscopic physical/mechanical properties. X-ray computed tomography (XRCT) and Synchrotron X-Ray computed tomography (SXRCT) are commonly used to analyze the microstructure of geo-materials. However, methane hydrates exist only at high pressure (up to several MPa) and low temperature (a few °C). This article describes the development of three experimental setups, which aim at creating methane hydrates in sandy sediment, adapted to XRCT and SXRCT observations. The advantages and drawbacks of each setup are discussed. The discussions focus on the effects of the choice of the system to control temperature and pressure on the quality of images. The obtained results would be useful for future works involving temperature and/or pressure control systems adapted to XRCT and SXRCT observations of various geo-materials.

Keywords: Methane hydrate-bearing sand, X-ray computed tomography (XRCT), synchrotron XRCT, experimental setups, scans conditions, high pressure, low temperature.

Introduction

Methane hydrates (MHs), being solid ice-like compounds of methane gas and water, are naturally formed at high pressure and low temperature in marine and permafrost settings. They are being considered as an alternative energy resource but also a source of geo-hazards and climate change (Collett et al. 2009). Depending on the characteristic particle size and the effective stress, different morphologies and pore distribution within natural sediments of methane hydrates, such as nodules/chunks, lenses/veins or pore-filling have been identified (Boswell et al. 2011; Dai et al. 2012). In the scope of methane gas production from methane hydrate-bearing sediments, currently, due to technical feasibilities, only pore-filling MHs at high hydrate saturation in sandy sediments are being considered. Most experimental works concern laboratory tests on synthetic samples because of challenges to get cored-intact methane hydrate-bearing sediment samples. In the objective of creating synthetic pore-filling methane hydrates in sandy sediments (to mimic natural sediments), different methods have been proposed such as the excess-gas, ice-seeding, or excess-water methods (Clayton et al. 2005; Priest et al. 2009; Waite et al. 2004). However, by using seismic wave velocities (Chand et al. 2004; Dvorkin et al. 2000; Dvorkin and Lavoie 1999; Dvorkin and Nur 1996; Helgerud et al. 1999), MHs are believed to exist in four idealized arrangements or “pore-habits”: cement, with grain-grain contacts; cement, with mineral coating; load-bearing and pore-filling. Physical and mechanical properties of sediments containing MHs depend considerably on methane hydrate morphologies and distribution within the pore space, which are thus of the essence for interpretation of geophysical data and reservoir-scale simulations in the scope of methane gas production (Taleb et al. 2018; Le et al. 2019; Nguyen-Sy

et al. 2019; Alavoine et al. 2020; Taleb et al. 2020). Therefore, pore-scale observations of MH morphologies and pore-habits in sandy sediments are crucial.

Laboratory X-ray computed tomography (XRCT) and Synchrotron X-Ray Computed Tomography (SXRCT) have been extensively used to investigate the 3D microstructure of gas hydrate-bearing sediments (Chaouachi et al. 2014, Kerkar et al. 2009; Kerkar et al. 2014; Ta et al. 2015; Zhao et al. 2015). Studying synthetic methane hydrate-bearing sand (MHBS) with these techniques is really challenging due to not only the need of special experimental setups (i.e. high pressure and low temperature should be maintained) but also to the poor image contrast between methane hydrate and water, which depends mainly on the difference of material density and atomic number. To improve XRCT/SXRCT image contrast, other gas/fluid (Tetrahydrofuran-THF, Carbon dioxide-CO_2 or Xenon-Xe) and/or saline water solutions (Sodium chloride-NaCl, Barium chloride-$BaCl_2$, Potassium iodide-KI) have been used (Chaouachi et al. 2014, Kerkar et al. 2009; Kerkar et al. 2014; Ta et al. 2015; Chen and Espinoza, 2018). By using gas/fluid different from methane, experimental setups are less complicated. For instance, there is no need of pressure control for the THF hydrate (THF hydrate can be formed at atmospheric pressure) while lower pressure and/or higher temperature are needed for studies of CO_2 or Xe hydrates. Note that gas hydrate morphology depends on the type of gas/fluid used. Furthermore, the phase boundary of methane hydrate formation is shifted depending on salt concentration contained in water Sloan and Koh (2008) and salt exclusion during gas hydrate formation increases the salt concentration in the remaining water.

Concerning XRCT image, spatial resolution mainly depends on the distances between the source, the object and the detector. Complex experimental setups of MHBS studies usually limit the image spatial resolution to avoid the collision between the source, the experimental setup and the detector. Morphologies and pore habits of methane hydrate formed in sandy sediments following the excess-gas method (MHs are formed by injecting methane gas into an unsaturated sandy sediment) have been investigated previously by Yang et al. (2015) and Zhao et al. (2015). Within voxel size of 25 μm, it was impossible to directly observe MHs as the voxel size was in the same order of magnitude as the size of the largest MH crystals. By using a conventional segmentation method based on gray levels (which are, as a first approximation, proportional to material density), methane hydrates were found to be formed at gas-water interfaces, floating between sand grains without coating grain surfaces (a water layer was found to envelop grain surfaces). However, image noise and partial volume effect (gray levels of voxels at interfaces of different phases are intermediate between the gray levels of the different phases) did influence the segmentation and the attributed phases (morphologies and pore habits of methane hydrates).

Note that reported XRCT scans were usually performed at the end of the gas hydrate formation process in sandy sediments as the scanning time is long (several hours). Within the high temporal resolution of SXRCT (a few minutes), the formation and growth of gas hydrate in sandy sediments could be captured over time.

In the present study, three experimental setups have been developed in the objective of investigating pore-scale morphologies and pore habits of MHs in sandy sediments via XRCT and SXRCT. Their designs aim at improving the image contrast and the image spatial resolution. As CT images can hardly differentiate pure water from methane hydrate, saline water (i.e. KI solution) was used to better distinguish the liquid phase and methane hydrate when both coexist. Furthermore, efforts have been made to enhance the image spatial resolution in order to distinguish methane hydrate from the liquid phase (either tap or saline water) on the basis of their morphology (regular water menisci or more complex geometry of MH). In the following sections, the optimization of XRCT scan conditions for MHBS is first described. Afterwards, the three experimental setups and their corresponding advantages and drawbacks are discussed.

Optimization of scan conditions

Absorption XRCT and SXRCT consist in exposing an object to X-rays from multiple orientations (by rotating the sample in this study) and measuring the intensity decrease for all source-detector paths. Gray levels of the obtained radiographic images, after calibration, quantify the attenuation of the sample, *i.e.* reflect the proportion of X-rays absorbed/scattered as they pass through the object. More precisely, X-ray attenuation follows a Beer-Lambert type law (Swinehart 1962), which involves the linear attenuation coefficient (μ). Different phases in the object can be well distinguished if their attenuation coefficients are significantly different from each other. Indeed, μ is a function of the energy of X-rays. In a polychromatic setup (as for

144 XRCT), the gray levels of the image result from a complex average of μ, which is
145 relative to the used energy range.

146

147 Lei et al. (2018) used potassium iodide solutions and in-line propagation-based
148 phase-contrast CT analysis of X-ray attenuation and diffraction for pore-scale
149 visualization of MHBS with XRCT. In the present study, theoretical ratios of μ of
150 different phases (methane gas, pure water, methane hydrate, saline water, quartz)
151 are first calculated in order to quantify the induced contrast between phases on the
152 image gray scale (see Figure 1). For the considered materials, sand grains are the
153 most absorbing objects while methane gas is the least absorbing. We thus plot the
154 absorption of the other phases (water, MHs and saline water) in a normalized scale
155 where 1 corresponds to grains and 0 corresponds to gaz. The XCOM program
156 established by the National Institute of Standards and Technology (NIST XCOM)
157 provides the mass attenuation coefficients (μ/ρ) of various compounds for various
158 values of photon energy. These data allowed plotting the curves corresponding to
159 water/quartz and methane hydrate/quartz shown in Figure 1. For the saline solutions
160 (*i.e.* Potassium iodide KI), the value of the mass attenuation coefficient of the solution
161 is obtained according to a simple addition:

162 $$\mu/\rho = \sum_i w_i \, (\mu/\rho)_i \qquad (1)$$

163 where w_i is the mass proportion of the component *i* (water or salt) and ρ is the unit
164 mass, being for water and Potassium iodide (KI) equal to 1 and 3.12 (Mg/m^3),
165 respectively. The results obtained for the KI solution of 2, 3.5 and 5 wt% are also
166 plotted in Figure 1. Note that the adopted density of quartz, methane gas, methane
167 hydrate and water is 2.65, 0.0007, 0.9 and 1 Mg/m^3 respectively.

Figure 1 shows that, for the whole considered energy range (10-200 keV, which corresponds to typical energies considered in a laboratory XRCT setup), there is almost no difference between the ratio of pure water/quartz and that of methane hydrate/quartz (red and black curves). The difference in gray level of these two phases is in the order of image noise (which typically varies from 2 % to 10 % of gray level range). That explains the difficulty in distinguishing methane hydrate from water in a XRCT image. For the case of KI solutions (blue curves), their ratios are significantly different from that of methane hydrate in the range of photon energy higher than 33 keV where an absorption edge is observed. At a concentration of 5 % for KI, the maximum ratio is close to 1 (*i.e.* saline solution absorbs almost as quartz) while at 2 % of concentration, the increase in contrast (allowed by the KI solution) is moderate. Therefore, saline water of 3.5 % of KI by weight was chosen in this study so that saline water can be optimally distinguished from both methane hydrate and sand grain. More precisely, for energies between 33 and 60 keV, the gray level of saline solution would be at equal distance from quartz and MH, optimizing the image contrast. Note that the laboratory XRCT source is a polychromatic source with a wide energy spectrum with a maximal energy corresponding to the prescribed electron beam acceleration voltage. However, its maximum intensity, due to the Bremsstrahlung effect, is somewhat below that maximum. Furthermore, to avoid beam hardening artifacts in XRCT images and more specifically to reduce X-rays bellow 33 keV, a copper filter (Cu) was used to eliminate low energy X-rays. Relative transmission of X-ray intensity $exp(-\mu_{Cu} \times t_{Cu} - \mu_{Al} \times t_{Al})$ of two cases of copper thickness (t_{Cu}), is also shown in Figure 1 (Aluminum tube thickness, t_{Al} is 2 x 0.89 mm). In the present study, a Cu filter with a thickness of 0.1 mm was used for the

193 scans to preserve a higher X-ray flux in the energy range of 30 – 100 keV where the
194 linear attenuation coefficient ratio of the KI solution at 3.5 wt% is well separated from
195 that of methane hydrate.

196

197 Preliminary scans at abovementioned optimized conditions (acceleration voltage of
198 source was 80 or 100 keV; 0.1 mm thick Cu filter) were done. Typical close views of
199 cross sections of 3D images obtained on mixtures of dry sand with either pure water
200 or saline water compacted in an aluminum tube (exterior diameter, $d_{ext.}$ = 6.45 mm;
201 thickness, t = 0.89 mm) are shown in Figure 2. For the case of sand wetted with pure
202 water, Figure 2a, the mean gray levels of each phase were determined from the gray
203 level profiles along the yellow line in Figure 2a, plotted in Figure 3a: G_a = 21100 (for
204 air, A); G_q = 22700 (for quartz, Q); G_w = 21600 (for pure water, W). Similarly, for the
205 case of sand wetted with saline water (Figure 2b), Figure 3b shows: G_a = 12400; G_q
206 = 14150; G_{sw} = 13400 (saline water, SW). The ratios of water, $R_{w/q}$ and of saline
207 water, $R_{sw/q}$ were calculated as follows:

208 $$R_{w/q} = (G_w-G_a)/(G_q-G_a) \quad (2)$$

209 $$R_{sw/q} = (G_{sw}-G_a)/(G_q-G_a) \quad (3)$$

210 According to profiles shown in Figure 3, $R_{w/q}$ is equal 0.3 while $R_{sw/q}$ equal 0.6.
211 Furthermore, it is expected that the ratio of methane hydrate/quartz is close to that of
212 water/quartz. These scan conditions should be then appropriate for MHBS scans,
213 with an optimal contrast between air, MH, saline water and quartz (relative gray
214 levels equal 0, 0.3, 0.6, and 1, respectively).

215

Unlike conventional laboratory XRCT, the so-called “pink beam” SXRCT makes use of a narrower energy spectrum, which is more concentrated around a mean energy. Details of effective linear attenuation coefficient has been defined in the work of Lei et al. (2018). Preliminary SXRCT scans (typical cross sections shown in **Erreur ! Source du renvoi introuvable.**) were performed at the Psiche beamline at the French synchrotron SOLEIL (King et al. 2016) run in pink mode with a mean energy of 44 keV. $R_{w/q}$ and $R_{sw/q}$ are 0.25 and 0.6 respectively (Figure 5). These values are close to the theoretical estimations at 44 keV (see Figure 1). Note that the Paganin filter (Paganin et al. 2002), designed to account for and partly correct phase contrast artifacts, has been used during the image reconstruction. It can also be noticed from profiles in Figures 3 and 5 that noise levels are significantly lower in SXRCT images than in XRCT ones.

Experimental setup investigations

Materials and methodology

The sediment used in this study was Fontainebleau silica sand (NE34). Classified as SP according to the Unified Soil Classification System (USCS), it consists of quartz grains having a diameter ranging from 100 to 300 microns. Tap water and saline solution (KI with concentration of 3.5 %) were used for the test. Standard purity of the used methane gas was 99.995 %. The characteristics of tap water provided by the supplier are: total chlorine 0.48 mg(Cl_2)/L; pH 7.7; electrical conductivity (at 25 °C) 609 μS/cm; total iron < 10 μg/L; total aluminum 53 μg/L. In the present work, we consider that the salinity and the total dissolved solids in the tap water are negligible.

Moist sand was first compacted by tamping in layers into an aluminum tube (exterior diameter, d_{ext} = 6.45 mm; thickness, t = 0.89 mm). Aluminum was chosen instead of beryllium as used in other studies (e.g. Lei et al. 2018) to facilitate the manipulation because of the toxicity of beryllium. The initial water content was fixed in the range between 10-15 % with an accuracy of ±0.1%. In the present work, we consider that the initial water content does not influence the quality of the obtained images. The average porosity (volume of gas and liquid phases divided by total volume of the sample) was estimated at 0.40 by segmenting several 3D images obtained on the samples at various locations (see Le 2019, for more details about the segmentation technique). Both high pressure and low temperature (2-3 °C; 7 MPa) were maintained for the MH formation.

To maintain low temperature, cooled air was circulated around the aluminum tube. Compressed air was cooled down by using a combination of chilled water (controlled by a cryostat) and a heat exchanger. Cooled air temperature, as well as sample temperature, were controlled via the compressed air flow rate (by imposing a compressed air pressure). Note that air was chosen instead of liquids for the temperature control to avoid additional X-ray absorption. In addition, preliminary experiments with wet sand showed an identical temperature (measured by thermocouples) in the air, outside of the aluminum tube, and that in the wet sand, at the center of the aluminum tube, at the same height.

Methane gas was injected into the sample to maintain a high methane gas pressure. It is supposed that methane gas pressure is constant in a closed system once the

MH formation is finished (no need of additional methane gas for further MH formation). Therefore, at the end of the MH formation when the media are supposed to be stable, there is no need to control methane gas pressure during the XRCT scans. However, when the purpose is to follow the MH formation over time by SXRCT scans, methane gas pressure needs to be controlled and maintained constant during the whole process.

The above thermal and pressure conditions were maintained during the laboratory XRCT scans, which lasted about 12 hours each to avoid MH dissociation. A generic view of various experimental setups developed in this purpose is shown in Figure 6. The sample was fixed on a turntable for scans. An Ultratom micro-tomography setup, from RX Solutions, using either a Hamamatsu L10801 micro-focus reflection (230 keV) or a Hamamatsu L10712 nano-focus (160 keV) transmission X-ray source together with a Paxscan Varian 2520V flat-panel imager (1920x1560 pixels^2, pixel size of 127 µm), was used for the laboratory XRCT scans. At an optimized Source Detector Distance (SDD), governed by the divergence of the X-Ray cone-beam of the X-Ray source in use, a smaller Source Object Distance (SOD) would provide a higher spatial resolution (or a smaller voxel size).

Furthermore, SXRCT scans were performed at the Psiche beamline at the French synchrotron SOLEIL (King et al. 2016) with a mean energy of 44 keV. Voxel size was 0.9 µm and the scan time 12-15 minutes. Paganin filter was optimized to limit the phase contrast at the interfaces between constitutive phases so that gray level of each phase in the images remains almost homogenous (apart from noise).

In the present study, three setups have been developed. The details of each of them, their advantages and drawbacks and the obtained results are presented in the following sections.

Experimental setup No. 1

Figure 7 shows the first setup used for XRCT scans of MHBS. A poly-methyl-methacrylate tube (PMMA tube; exterior diameter, d_{ext} = 24 mm; thickness, t = 3.5 mm) was fixed around the aluminum tube for the cooled-air circulation from its bottom to its top. A manometer was fixed at the top of the aluminum tube to monitor methane gas pressure in the tube. The aluminum tube height was chosen to avoid collision between the manometer and the X-ray source during the scan (the distance from the turntable to the top of the aluminum tube is 430 mm, see Figure 7). Note that both XRCT sources available on the Ultratom setup can be used. A thermocouple was installed between the aluminum tube and the PMMA one at the middle of its height. Methane gas at 7 MPa was injected during the MH formation by a pressure controller, which was connected to a gas flowmeter. These conditions were maintained during two days for the MH formation. At the end of the MH formation, pressure controller and gas flowmeter were removed, and all the valves were closed prior to the transportation of the whole system to the XRCT room.

A cooling gel was wrapped around the PMMA tube during the cell transportation (which lasted about five minutes during which the cooled-air circulation had to be cut

312 off) to avoid MH dissociation. The cooled-air circulation around the aluminum tube
313 was reset as quickly as possible once the cell was installed inside the XRCT room.
314 Sample pressure and temperature were verified before the scan. The Source Object
315 Distance (SOD) was limited by the exterior diameter of the PMMA tube (SOD $\geq$ 20
316 mm to maintain a security distance of 8 mm). Dry compressed-air flow was shifted
317 towards the PMMA tube to avoid water condensation during scans (anti-
318 condensation system). Both aluminum and PMMA tubes were rotated together to
319 maintain sample temperature during the scan. The soft tube bringing cooled air from
320 the heat exchanger to the PMMA tube needed to be flexible and long enough to
321 rotate with the PMMA tube.

322

323 Twelve tests have been performed with this setup, among which however, only a few
324 gave images exhibiting good enough quality to be used to characterize
325 microstructure (about 40 %). Indeed, it turned out that the cell slightly vibrated during
326 the scans because of the turbulent cooled-air flow. These vibrations induced
327 fluctuations of the CT geometry whose amplitude were too large for an accurate CT
328 reconstruction. The obtained 3D images were thus blurred, with very unsharp edges.
329 An example of an unsuccessful scan is shown in Figure 8. Gray levels within the
330 constitutive phases, including grains, were not homogenous. MH morphology
331 observation was then impossible. An example of a successful scan is shown in
332 Figure 9 (voxel size was 5 µm). The image shows an assembly of sand grains (light
333 gray), the pore space filled with methane gas (black) and methane hydrates (gray).
334 MHs can be observed at grain contacts and also on grain surfaces. The mean gray
335 level of each phase was determined from the gray level profiles (as illustrated in
336 **Erreur ! Source du renvoi introuvable.**10): G_a = 22500 (for air, A); G_q = 33000 (for

quartz, Q) and G_{mh} = 26500 (for methane hydrate, MH). The ratio $R_{mh/q}$ *is* equal to 0.38, similar to the expected ratio. Furthermore, the standard deviations of the quartz and methane gas phases are close (700). Signal to noise ratio (SNR) was estimated at (33000 – 22500)/700 = 1/0.067.

Experimental setup No. 2

In order to improve the image spatial resolution, the setup No. 2 (shown in Figure 11) has been designed. First, to further reduce the SOD, the PMMA tube (used in the setup No. 1) was removed. The nano-focus source was used instead of the micro-focus one, and the aluminum tube was placed closer to it during the scans: SOD was 8 mm instead of 20 mm in the setup No. 1. A Polyvinyl Chloride (PVC) support was fixed to the source and enveloped the aluminum tube. Temperature control was ensured by a circulation of cooled air inside this PVC support, again from the bottom to the top. A thin Kapton film was used to thermally isolate the source (and in particular its thin window) and to protect it from the cooled air. Within this system, only the aluminum tube was rotated during the scans while the PVC support was fixed. A smaller air flow rate (compressed air pressure was about 200 kPa compared to 360 kPa for the setup No. 1) was needed to maintain a similar sample temperature. Actually the heat flux from ambient air through the soft tube walls, between the heat exchanger and the cooled-air inlet, was lower (in particular because of a shorter soft tube length). In addition, the manometer was fixed at the bottom of the cell and the aluminum tube height was reduced to 320 mm (this minimal length being constrained by the diameter of the nano-focus source). These

361 modifications allowed significantly reducing the amplitude of the vibrations of the
362 aluminum tube during scans.

363

364 Methane hydrates were equally formed in sandy sediments in the laboratory then
365 transported to the XRCT room for scans. The PMMA tube (used for setup No. 1) was
366 placed around the aluminum tube to initially form MHs. Compared to the setup No. 1,
367 the installation of the cell in the XRCT room was more complicated as cooled air can
368 only be circulated when the aluminum tube was enveloped by the PVC support.
369 Sample temperature was maintained by a cooling gel wrapped directly around the
370 aluminum tube during its installation. A thermocouple, fixed on the PVC support (see
371 Figure 11), was used to measure the sample temperature close to the scanned zone.

372

373 As for the first setup, among the ten scans preformed with the second setup, only a
374 few provided images with good quality (about 40 %), again because of cell vibrations.
375 An example of successful result is shown in Figure 12 (voxel size was 3.5 µm). MH
376 was more difficultly distinguished from methane gas even with a better image spatial
377 resolution compared to the setup No. 1 (see Figure 9), because in particular of a
378 poorer signal to noise ratio. $R_{mh/q}$ and SNR were estimated at 1/3 and 1/0.085
379 respectively (Figure 13).

380

381 Another possible reason, to explain the heterogeneity of gray levels in the phases, is
382 related to the heterogeneous and porous structure of the PVC support. Indeed, X-
383 rays passed through a thin PVC layer serving for thermal isolation before being
384 captured by the detector. During the calibration stage of the CT scans, which consists

in recording various radiographs without sample, the PVC layer crossed by X-rays is not exactly at the same position as during the scans with the sample, which induces additional artifacts. For a further development of setup No. 2, another, more homogeneous material (such as PMMA) should be used between aluminum tube and detector. Actually, PVC was chosen in this study because manufacturing the complex-shaped support with PVC was easier (compared to PMMA).

Experimental setup No. 3

Within the two first setups, methane hydrates were first formed outside the tomography room and XRCT scans were performed only when the MH formation was stabilized. During the scans, the cell was closed and the temperature was maintained. Setup No. 3 was primarily developed for SXRCT scans which allow one to continuously follow the formation and evolution of MHs. For this reason, methane gas needs to be supplied and its pressure to be monitored during the scans.

Figure 14 shows the schematic view and a picture of the setup No. 3. A small methane gas bottle (volume of 40 mL) was connected to the methane gas inlet of the cell via a pressure reducer, which reduced the methane gas pressure from 13 MPa inside the bottle to 7 MPa at the gas inlet. This system was used to maintain methane gas pressure in the sample constant at 7 MPa (±0.1 MPa) during the MH formation and scans.

Cooled air was circulated between the aluminum and a PMMA tube, similar to the one used in the setup No 1 but somewhat smaller and thinner (exterior diameter, d_{ext} = 23 mm; thickness, t = 2 mm), for the temperature control. The cooled-air inlet was, in this setup, at the top of the PMMA tube. The PMMA tube was fixed at its top and thus did not rotate during the scans. The compressed air pressure was in the same order as that used for the setup No. 2. In addition, the aluminum tube height was reduced to 180 mm. Two thermocouples, inserted into the PMMA tube to measure the air temperatures close to the air inlet and outlet, showed a rather stable temperature difference of 1.5 – 2.0 °C during the scans.

Figure 15 shows a preliminary result obtained by XRCT, with a voxel size of 4 µm. The micro-focus source was used because the geometry of the tube does not allow high resolution. This 15-hour scan was started 28 hours after the start of the experiment, during which temperature and pressure were controlled, when the formation of MH was considered to be stabilized. MH morphologies (crystals/layers) were clearly observed over grain surfaces. Furthermore, $R_{mh/q}$ and SNR were 0.3 and 1/0.095 respectively (Figure 16). It can be seen that the $R_{mh/q}$ and SNR were in the same order for the three experimental setups. The difference was that successful scan ratios were lower for the two first setups due to cell vibration while this problem was well resolved by using the third one: all five XRCT tests were successful. The setup No. 3 is however not compatible with higher resolution XRCT imaging because of the large diameter of the PMMA tube.

The setup No. 3 was also successfully used to perform SXRCT scans. An example is shown in Figure 17 (voxel size was 0.9 µm). Really small hydrate particles, formed at

433 the sand grains surface, can be clearly observed. $R_{mh/q}$, $R_{sw/q}$ and SNR were 0.27,
434 0.73 and 1/0.080, respectively (Figure 18). The ratios ($R_{mh/q}$, $R_{sw/q}$) calculated on the
435 image are close to the theoretical ones. A small increase of salt concentration in the
436 remaining saline water during the MH formation caused a slightly higher $R_{sw/q}$ value.

437

438 Furthermore, within the high temporal resolution of SXRCT, the evolution of methane
439 hydrate formation could be followed with time. Figure 19 provides vertical cross-
440 sections through the sample (note that previously shown cross-sections were
441 horizontal) at a same position at various times. Water was initially located at the
442 contacts of sand grains because of the capillary suction (Figure 19a). The air-water
443 interface can be easily identified by the concave meniscus. At 0.8 h from the
444 application of MH formation conditions, these interfaces became irregular and the
445 concave meniscus disappeared. In addition, a thin layer (of water or methane
446 hydrate) appeared on the surface of the grain. As water and methane hydrate have
447 similar gray levels and cannot be distinguished by gray levels, the evolution of their
448 morphology can be used. Actually, irregular interface between the gas phase and
449 water or hydrate phase suggests that this later became a rigid phase (i.e. methane
450 hydrate). Besides, the thin layer appeared on the sand grain surface should
451 correspond to methane hydrate as suggested by Chaouachi et al. (2015). It should
452 be noted that some water was moved out of this area between t = 0.3 - 0.8 h. We can
453 then expect that at 0.8 h, methane hydrate was formed at methane gas/water
454 interfaces and at the sand grain surface; MH layers became thicker with time as
455 shown in the Figure 19.

456

Discussions and recommendations

Three experimental setups were developed for pore-scale morphology and pore-habit investigations of MHs in sandy sediments via XRCT and SXRCT. The image spatial resolution was well improved by using SXRCT instead of XRCT. However, SXRCT scans are costly and access time is very limited. Furthermore, by using saline water, methane hydrates could be well distinguished from the remaining water during the MH formation (Figure 17) while for the case of tap water (e.g. Figure 19), methane hydrates and water could only be distinguished from each other via the kinetics of MH formation (MH crystals or layer were grown over time) or via the interface roughness (smooth interface between liquid and gas due to interfacial tension). However, due to the shift of the phase boundary of methane hydrate formation for saline solution, the sample temperature needed to be maintained at a lower temperature compared to that for water (1-2 °C lower at 7 MPa).

In previous studies where gas hydrate morphology in sediments were investigated, other gas/fluid (THF or Xenon) was used to facilitate the gas hydrate formation because only temperature control (Kerkar et al. 2009) or pressure control (Chen and Espinoza 2018) was required. In the present work, as methane hydrates were investigated, both low temperature and high pressure were required. Furthermore, in order to maintain a low temperature, liquid was usually used in previous studies (Chaouachi et al. 2015; Ta et al. 2015; Zhao et al. 2015; Le et al. 2020). That would avoid the system vibration induced by air flow, as observed in the present work. However, X-ray absorption of water would decrease the image's quality. Furthermore, voxel size in XRCT images, in these studies, was quite large, in a range

of 20 µm to 30 µm due to complex and bulky experimental setups, which were required to control both temperature and pressure (Ta et al. 2015; Yang et al. 2015; Zhao et al. 2015). Within such resolution, small particles of MHs could not be observed. Furthermore, the partial volume effect was important. In the present work, a voxel size of 4 µm was obtained by the setup No. 3 with a very good image's quality, even in a laboratory CT setup, MH morphologies (crystals, layers) were thus clearly observed.

Besides, Lei et al. (2019) used a Peltier plate for temperature control. Yet, a temperature gradient of 4 °C was measured between the top and bottom of the sample (about 54 mm height), *i.e.* 0.08 °C/mm. By using cooled air in this study, the temperature gradient over 150 mm of the tube height was about 2 °C, *i.e.* 0.013 °C/mm which favors the homogeneity of MH formation in the sample. Moreover, by using a small methane gas bottle in this study, associated with a pressure reducer, methane gas pressure was maintained constant during the whole MH formation process.

Among the three experimental setups developed in the present study, the third one was the most optimized. Actually, the aluminum tube height was shortened to minimize the vibration induced by the air flow. The setup No. 2 has the best spatial resolution for XRCT scans (voxel size equals to 3.5 µm) but its experimental procedure is the most delicate. Besides, the setup No. 2 was compatible only with the Nano-focus source while the two others can be used for all types of X-ray source.

Concerning the pressure control system, the sample can be disturbed during the system transportation to the XRCT room in the case of the two firsts setups. However, it avoids occupying the room during a long period. The setup No. 3 (using a small methane gas bottle) is the best choice for SXRCT scans. It however requires a setup compatible with large and heavy samples, as the one available on the Psiche beamline.

Conclusions

The paper describes the scan condition optimizations and the developments of special experimental setups to investigate pore-scale morphologies and pore-habits of MHBS via XRCT and SXRCT.

Based on theoretical attenuation coefficient ratios between phases, XRCT scan conditions were optimized (scan energy, filter thickness and saline water solution). Preliminary XRCT and SXRCT scans performed on compacted sand wetted with pure water or saline water confirmed the theoretical estimations.

Afterward, three experimental setups were developed in the objective of improving the image spatial resolution for pore-scale morphology and pore-habit investigations of MHs in sandy sediments via XRCT and SXRCT. The details of temperature and gas pressure controls were presented. The results obtained for each experimental setup allowed evaluating its performance to observe the morphologies and pore-habits of MHBS. The experimental setup No. 3 seems to be the most appropriate.

Sample temperature was controlled by circulating cooled air between the aluminum and the PMMA tube which is fixed at its top. Attention was paid to minimize the cell vibration induced by cooled air flux.

The choices of temperature and pressure controls presented in the present work can be useful for further studies on MHBS as well as other geo-materials involving a control of temperature and/or gas pressure during XRCT/SXRCT scans.

Acknowledgement

The authors would like to express their great appreciation to the French National Research Agency for funding the present study, which is part of the project HYDRE "Mechanical behavior of gas-hydrate-bearing sediments" –ANR-15-CE06-0008.

SXRCT images were recorded at the Psiche beamline of Synchrotron Soleil in the context of proposal 20181629.

We also would like to express our sincere thanks to Marine Lemaire and Emmanuel Delaure for their technical support.

Lists of figures

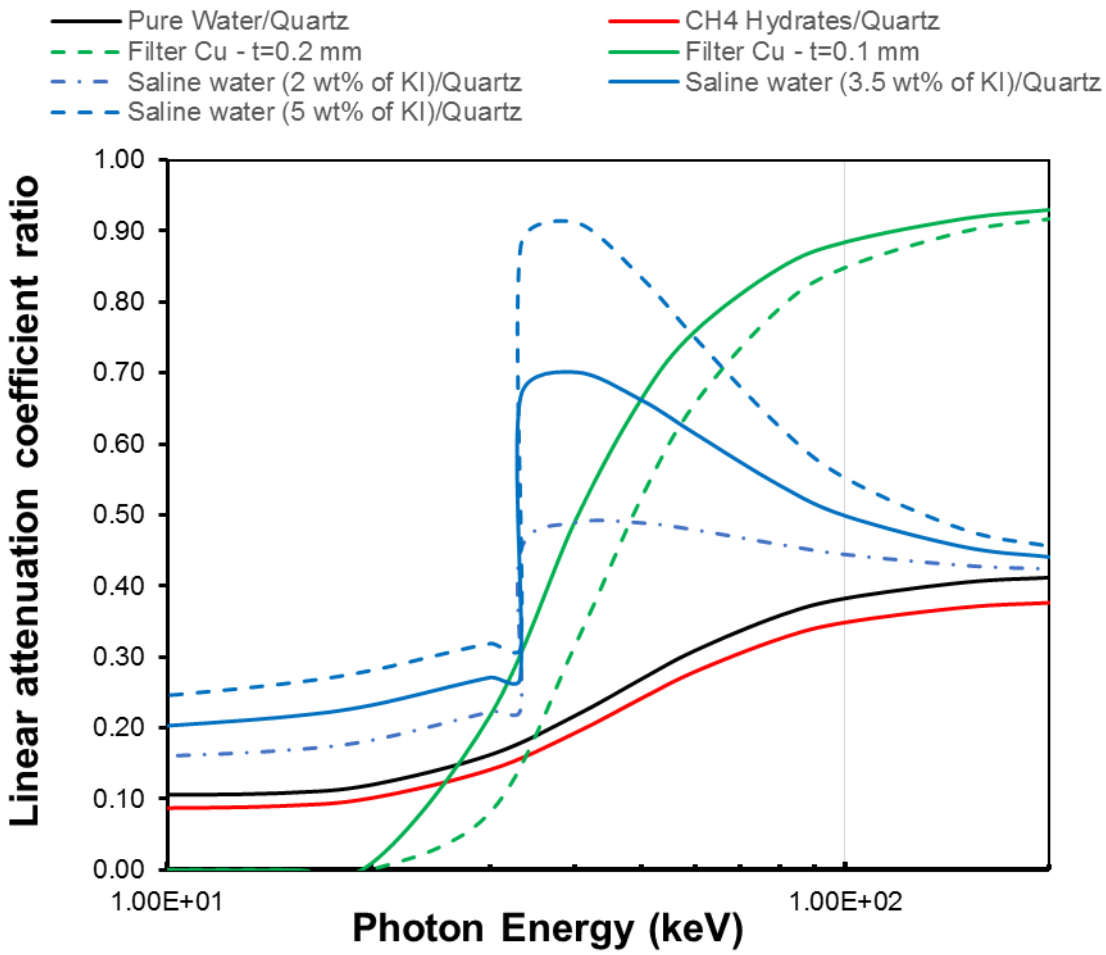

Figure 1. Linear attenuation coefficient ratio between phases, and X-Ray transmission through Cu filter, versus photon energy.

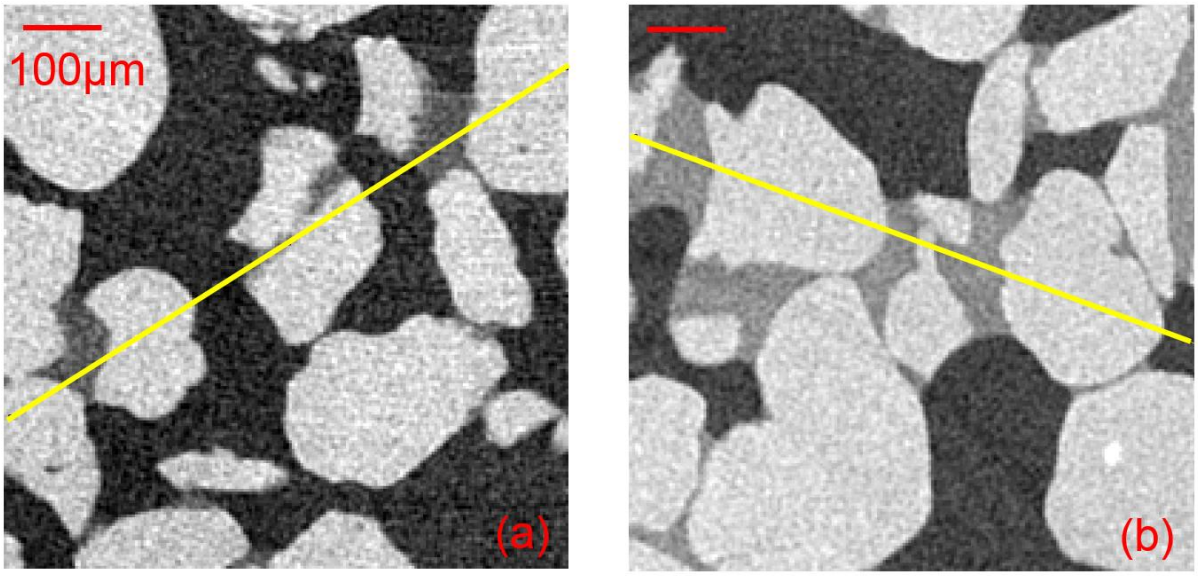

549 Figure 2. XRCT images of unsaturated sand with (a) pure water; (b) saline water.

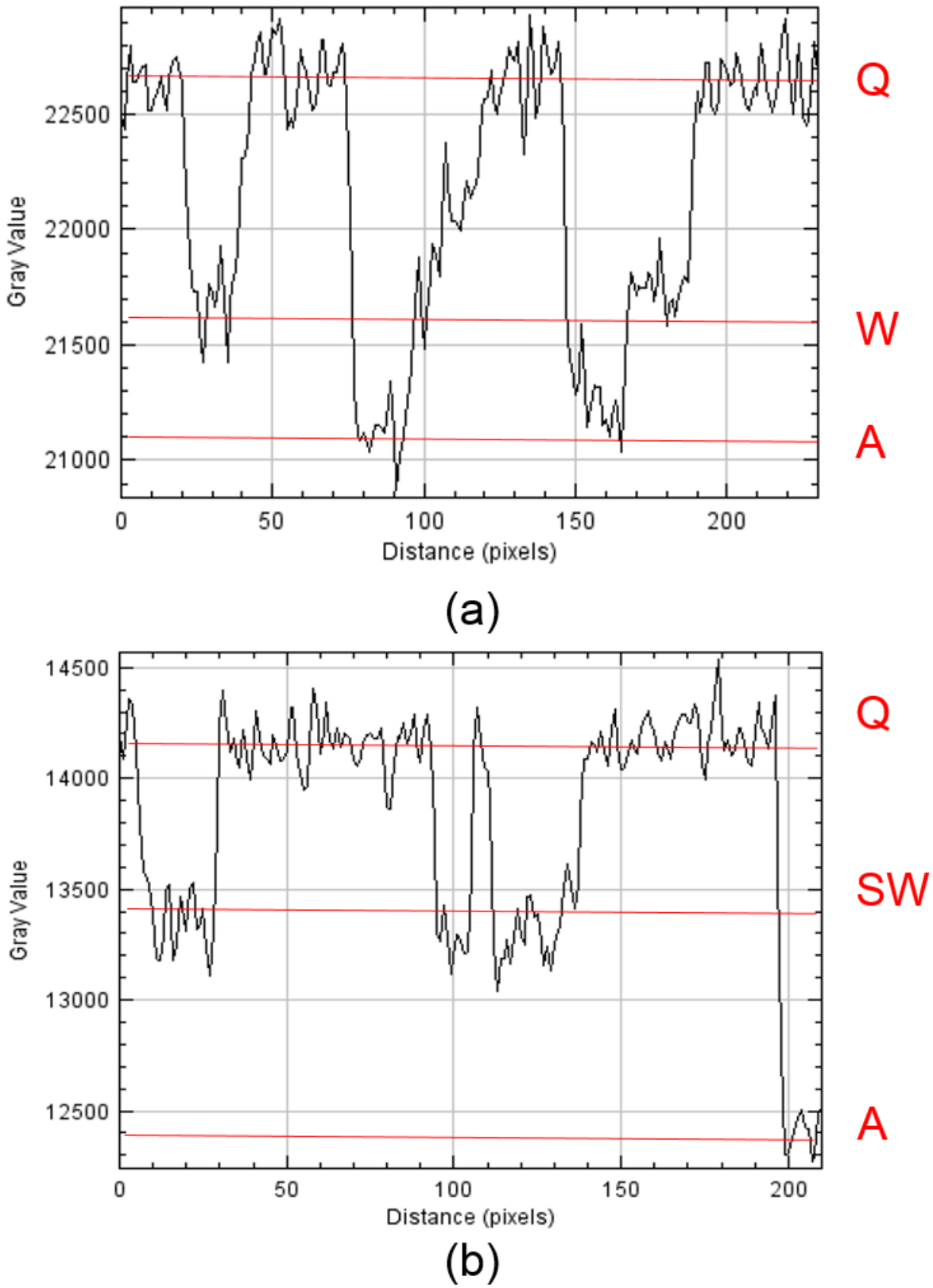

550

551 Figure 3. Gray level profiles along yellow lines in Figure 2: (a) water/quartz; (b) saline

552 water/quartz.

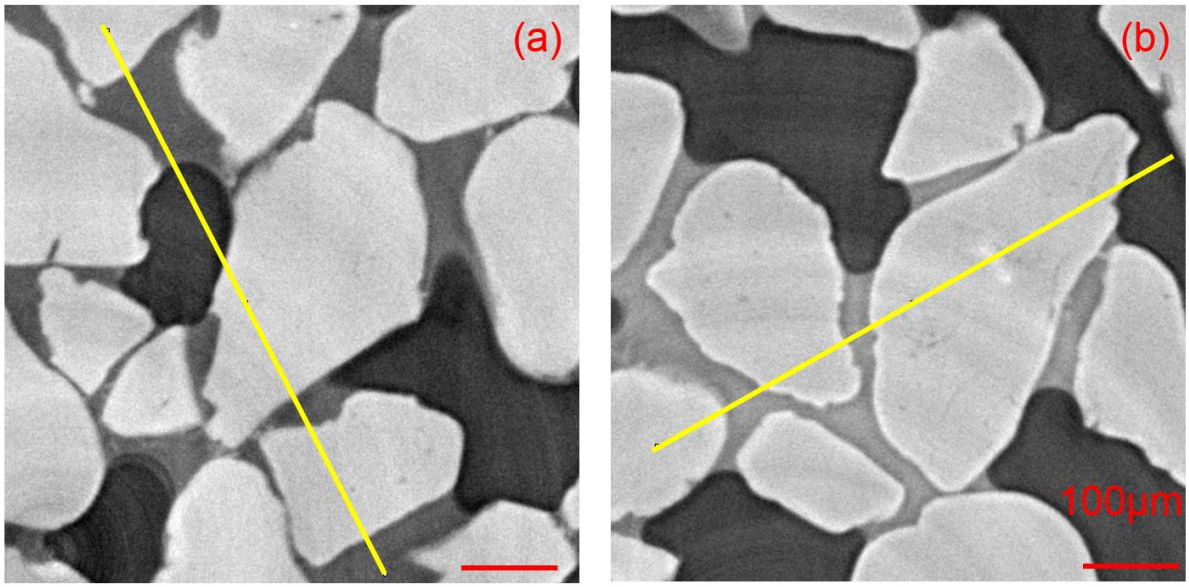

553

554 Figure 4. SXRCT images of unsaturated sand with (a) pure water; (b) saline water.

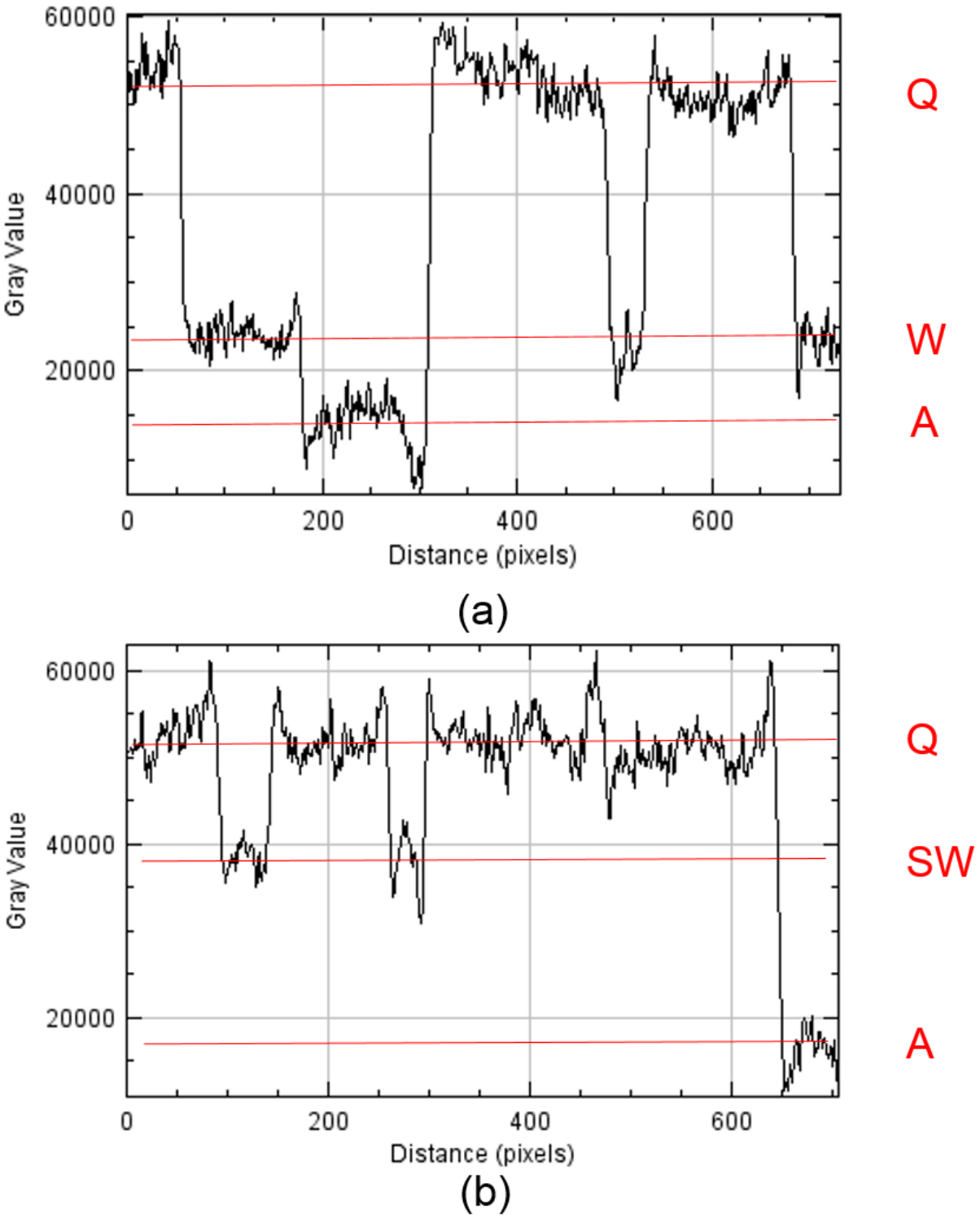

555

556 Figure 5. Gray level profiles along yellow lines in Figure 4: (a) water/quartz; (b) saline

557 water/quartz.

558

559

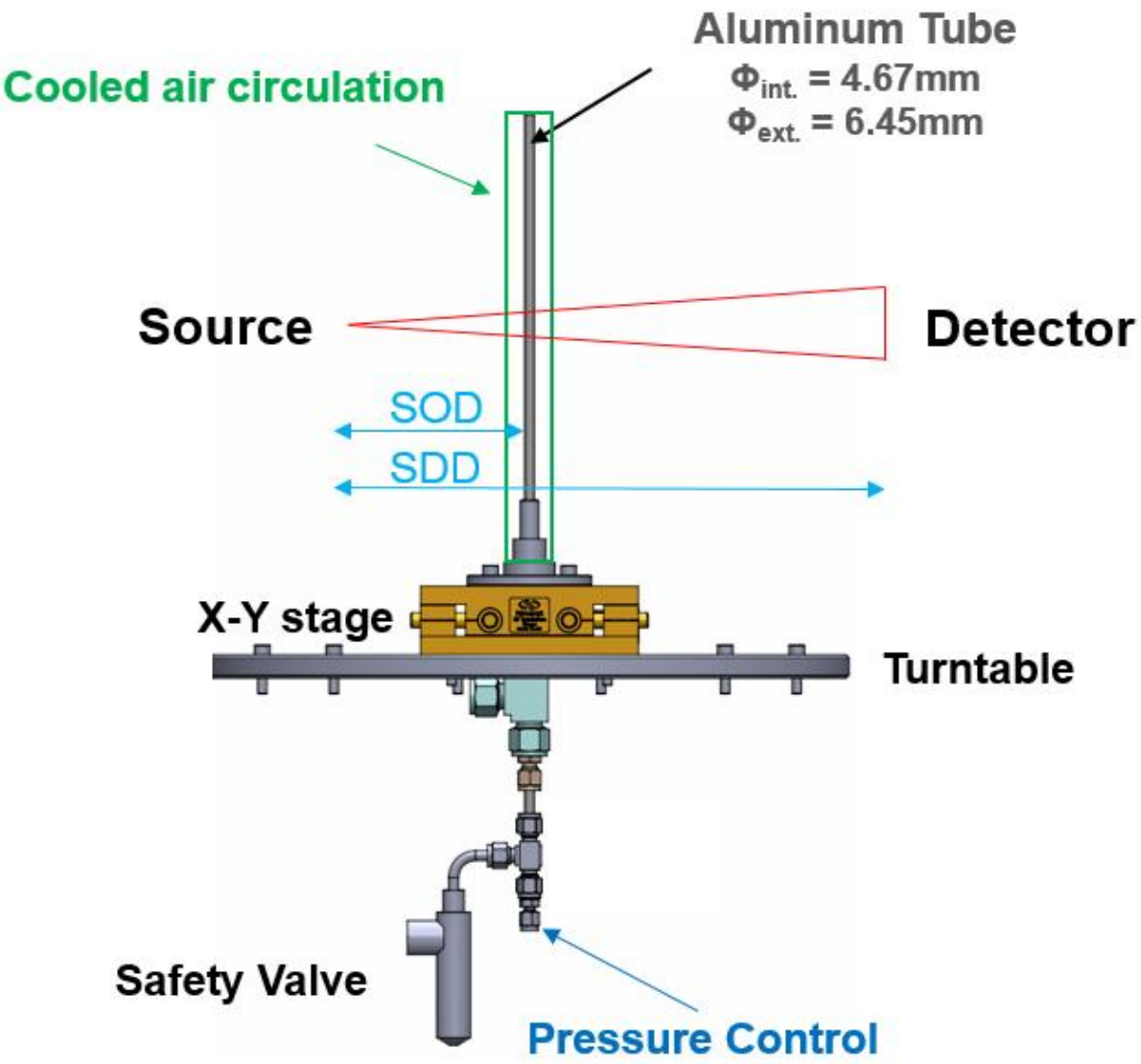

Figure 6. Experimental setup principles for XRCT scans of MHBS. SOD: Source Object Distance; SDD: Source Detector Distance.

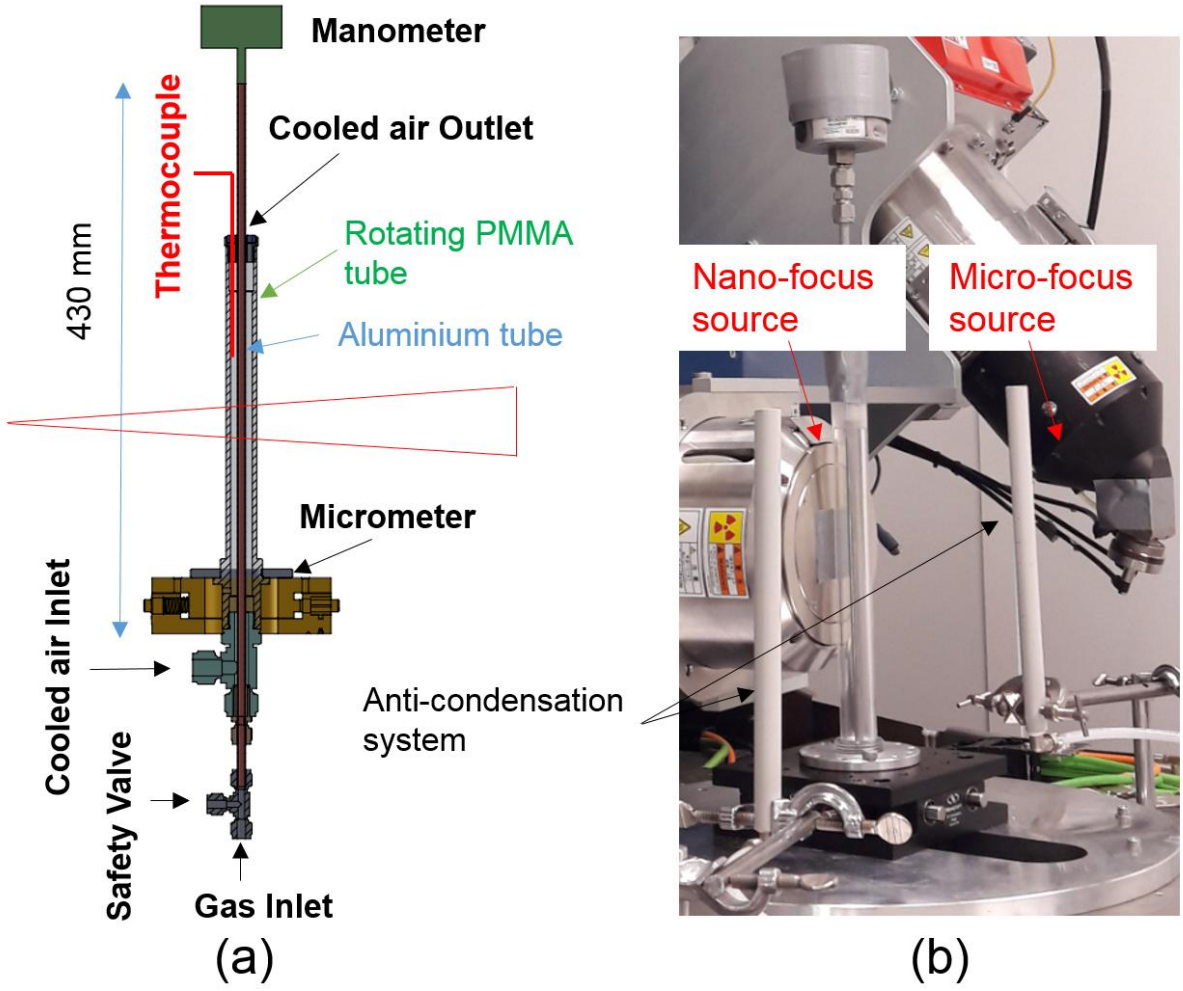

Figure 7. Experimental setup No. 1: (a) Schematic view; (b) picture.

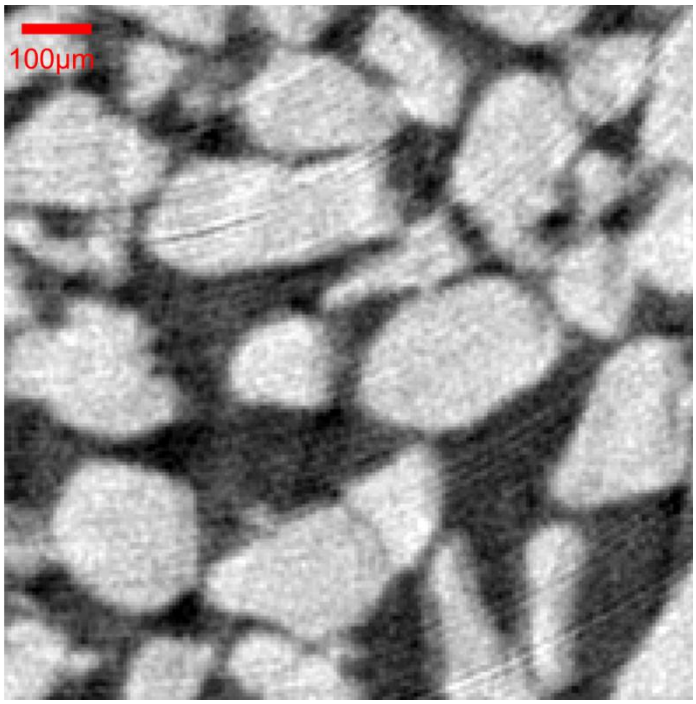

Figure 8. Example of image of an unsuccessful scan due to the cell vibration, obtained with the experimental setup No. 1. Voxel size: 5µm.

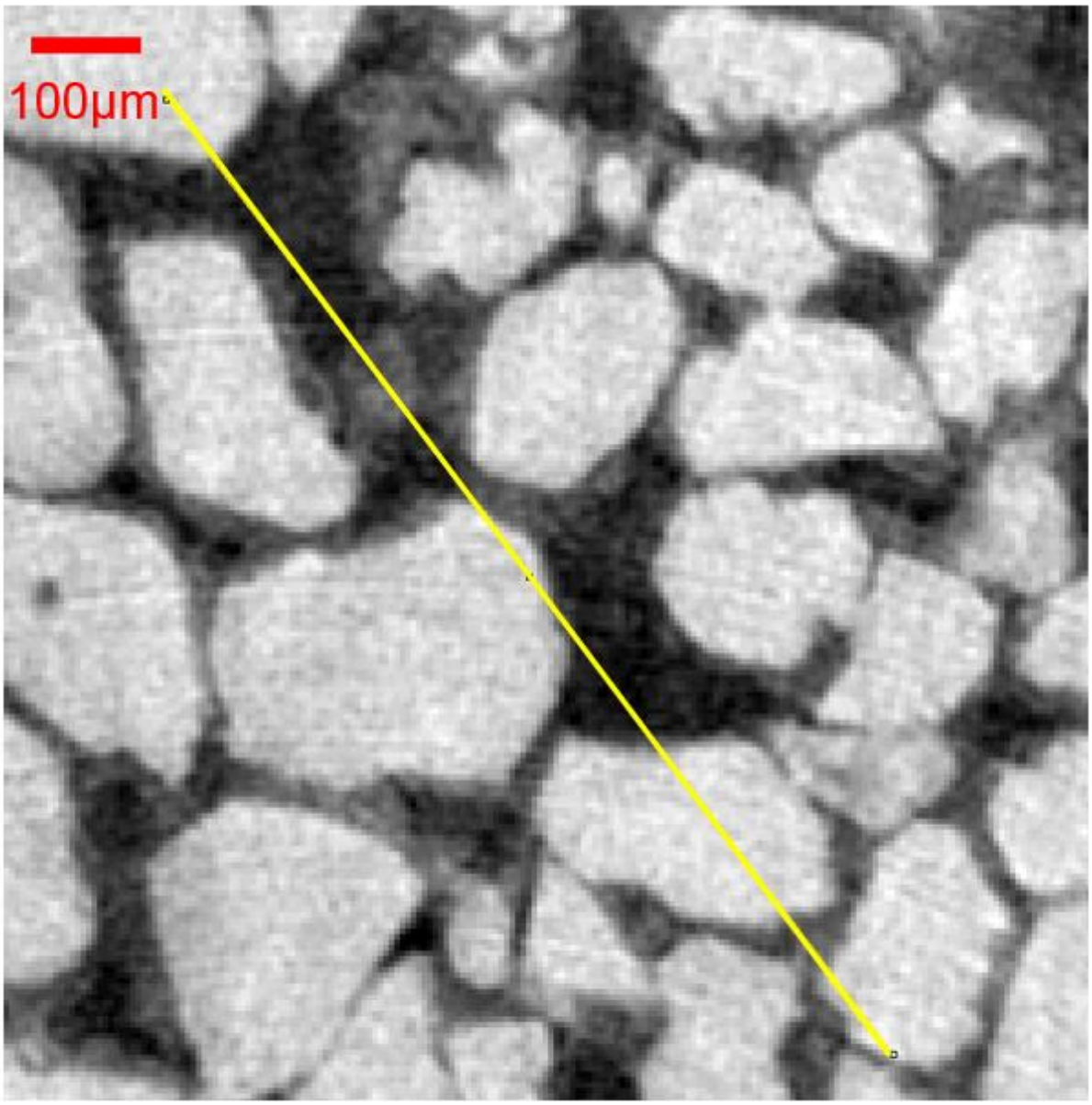

Figure 9. Example of image of MHBS obtained with the setup No. 1. Voxel size: 5µm.

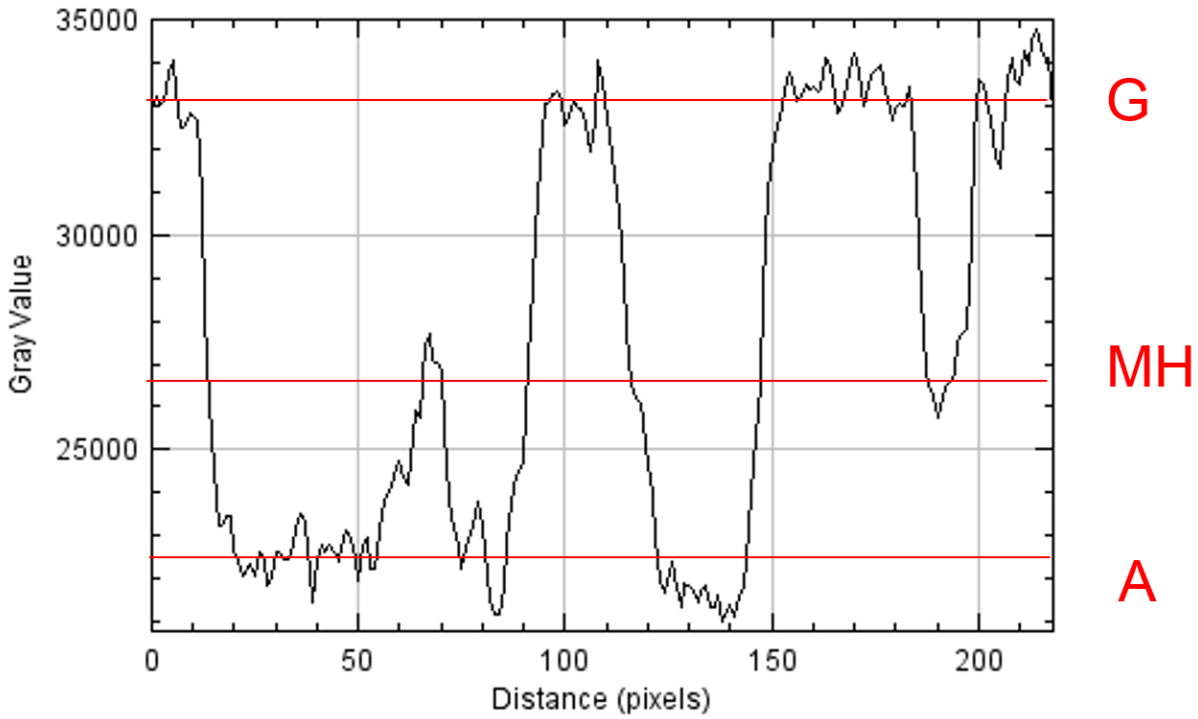

575

576 Figure 10. Gray level profile along yellow line in Figure 9.

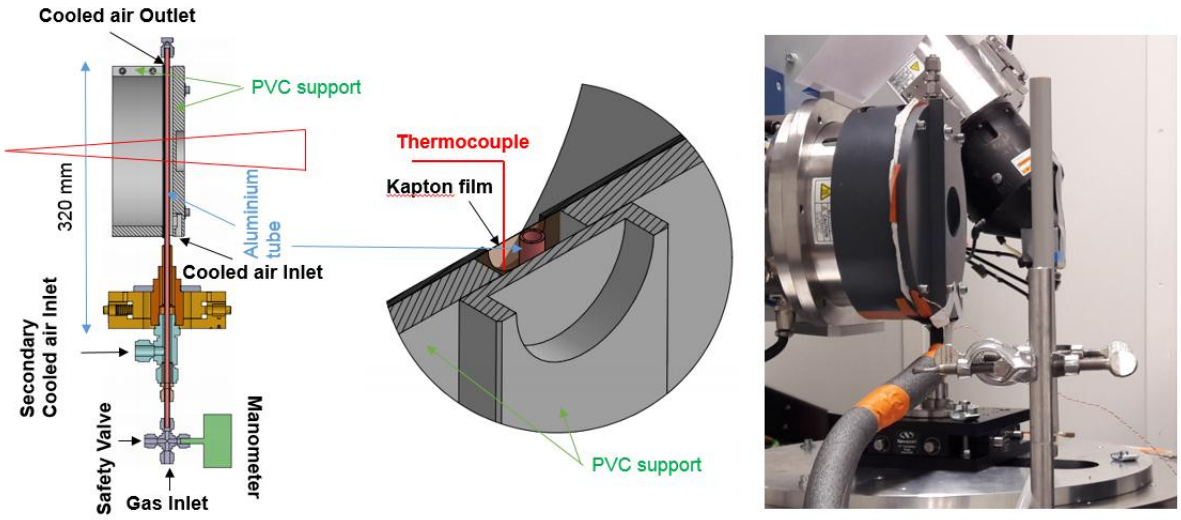

(a) (b) (c)

577

578 Figure 11. Experimental setup No. 2: (a), (b) Schematic view; (c) picture.

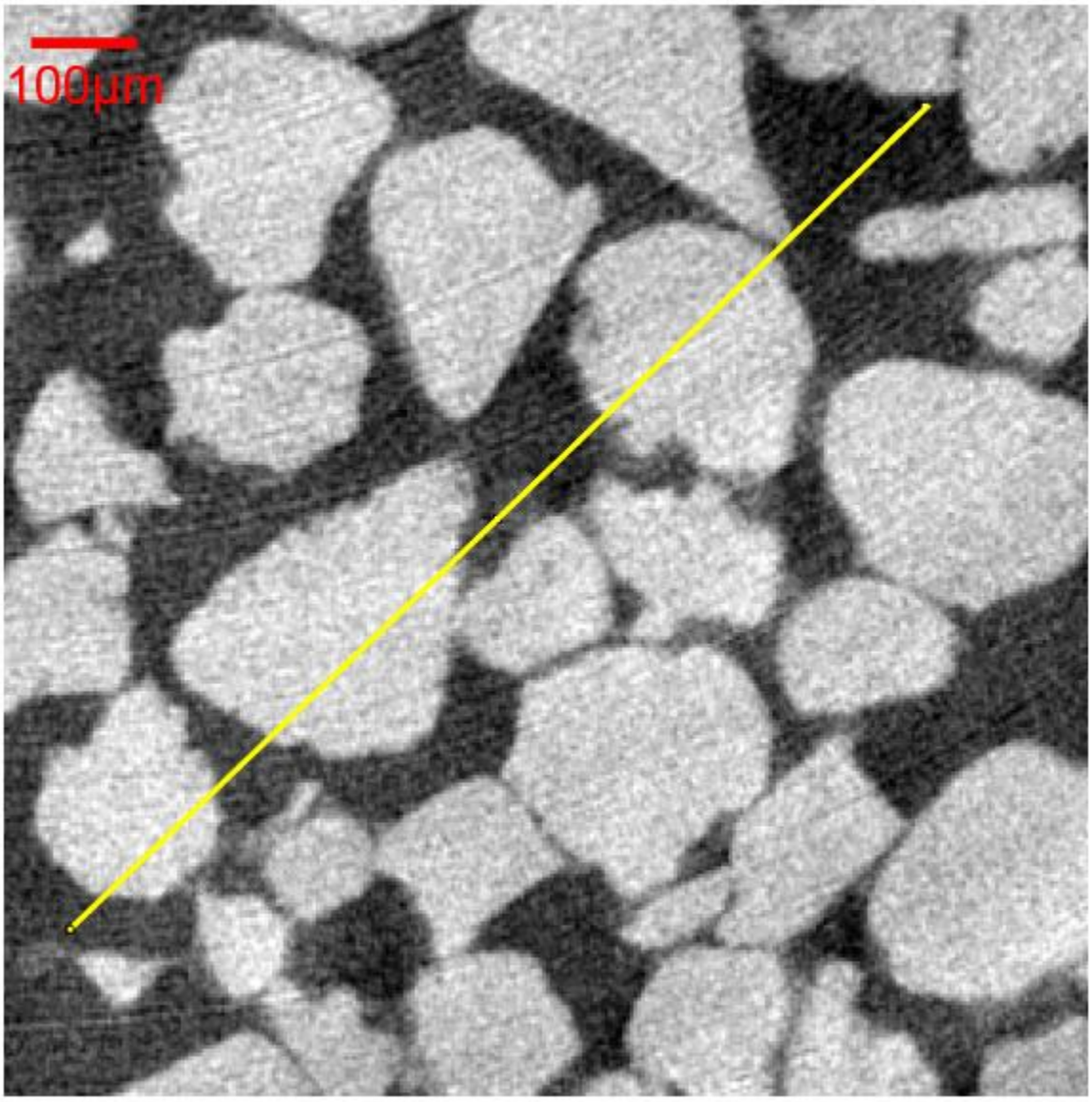

579

580 Figure 12. Example of image of MHBS obtained with the setup No. 2. Voxel size: 3,5

581 µm.

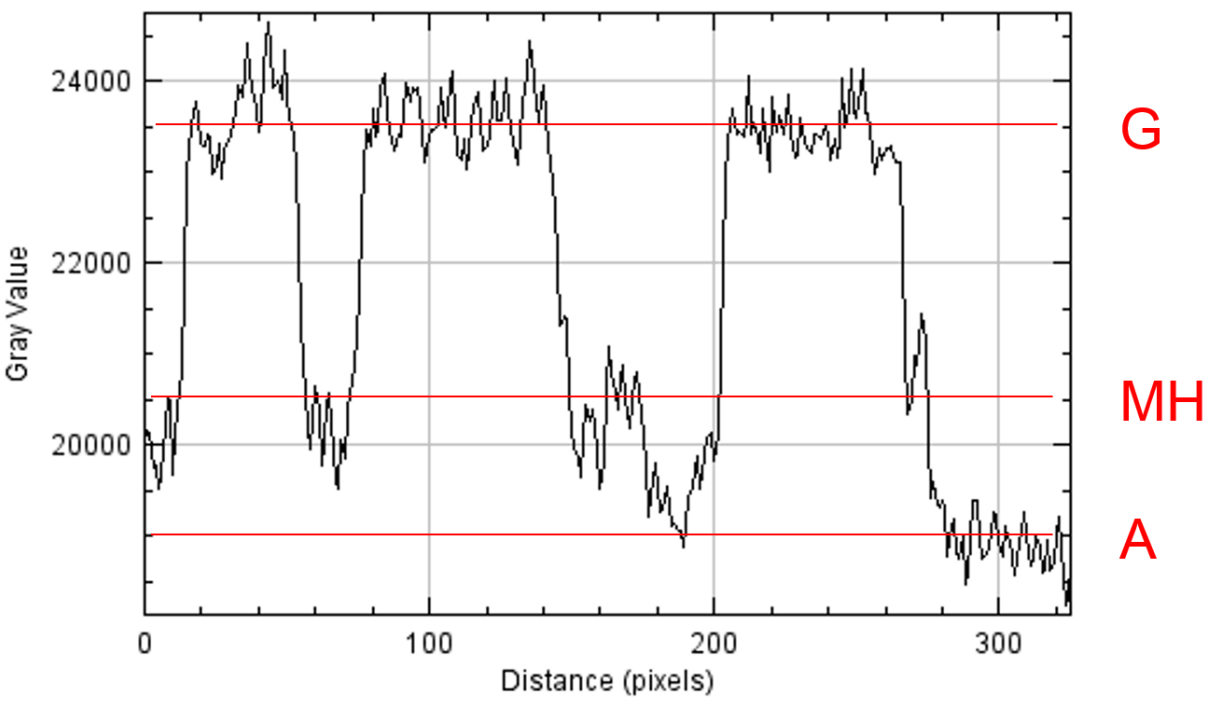

582

583 Figure 13. Gray level profile along yellow line in Figure 12.

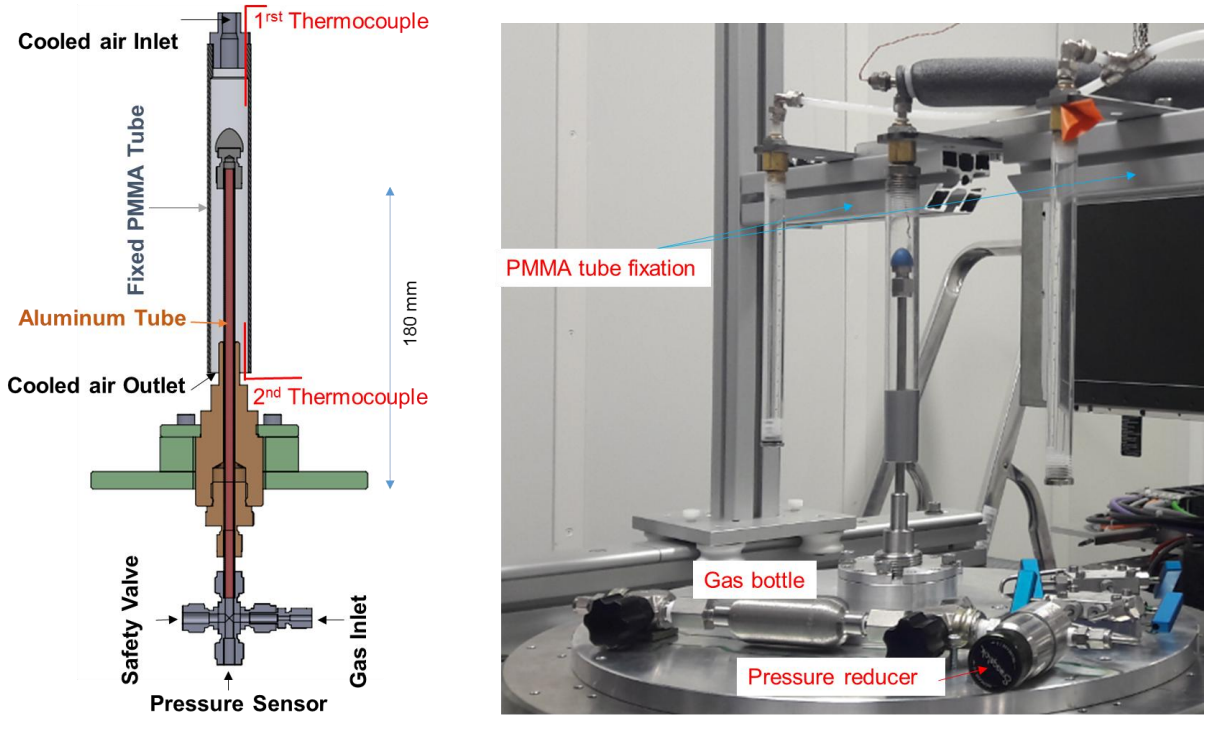

584

585 Figure 14. Experimental setup No. 3: (a) Schematic view; (b) picture.

586

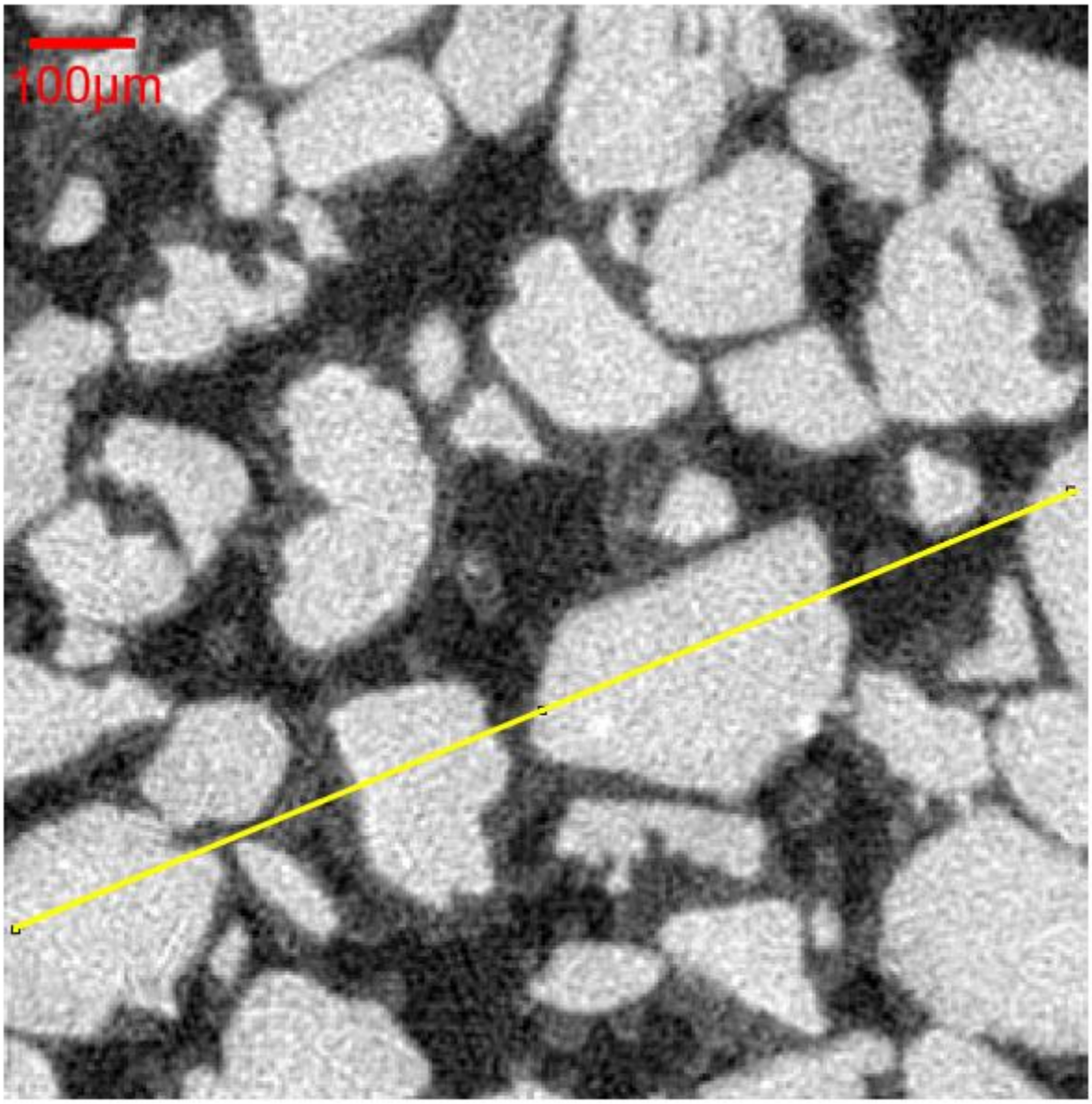

Figure 15. Example of XRCT image of MHBS obtained with the setup No. 3. Voxel size: 4 µm.

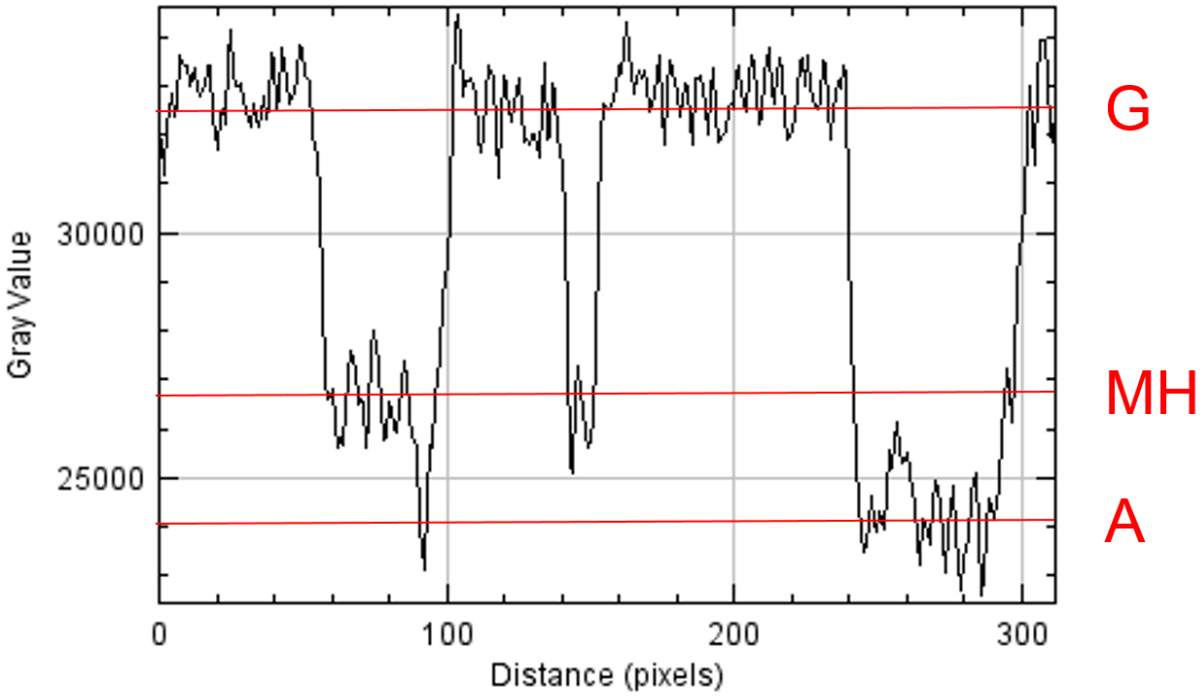

592

593 Figure 16. Gray level profile along yellow line in Figure 15.

594

595

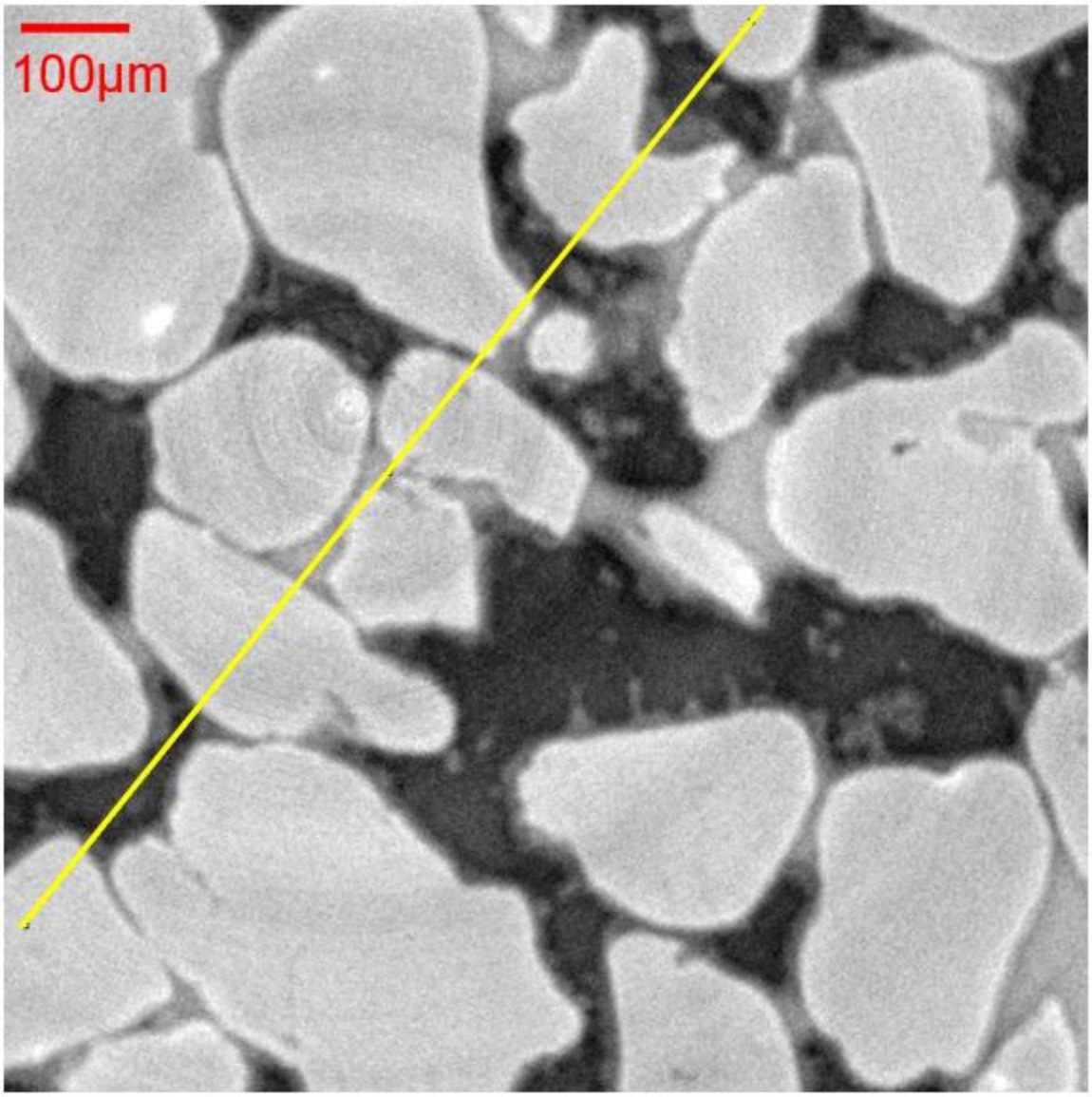

596

597 Figure 17. Example of SXRCT image of MHBS obtained with the setup No. 3. Voxel

598 size: 0.9 µm.

599

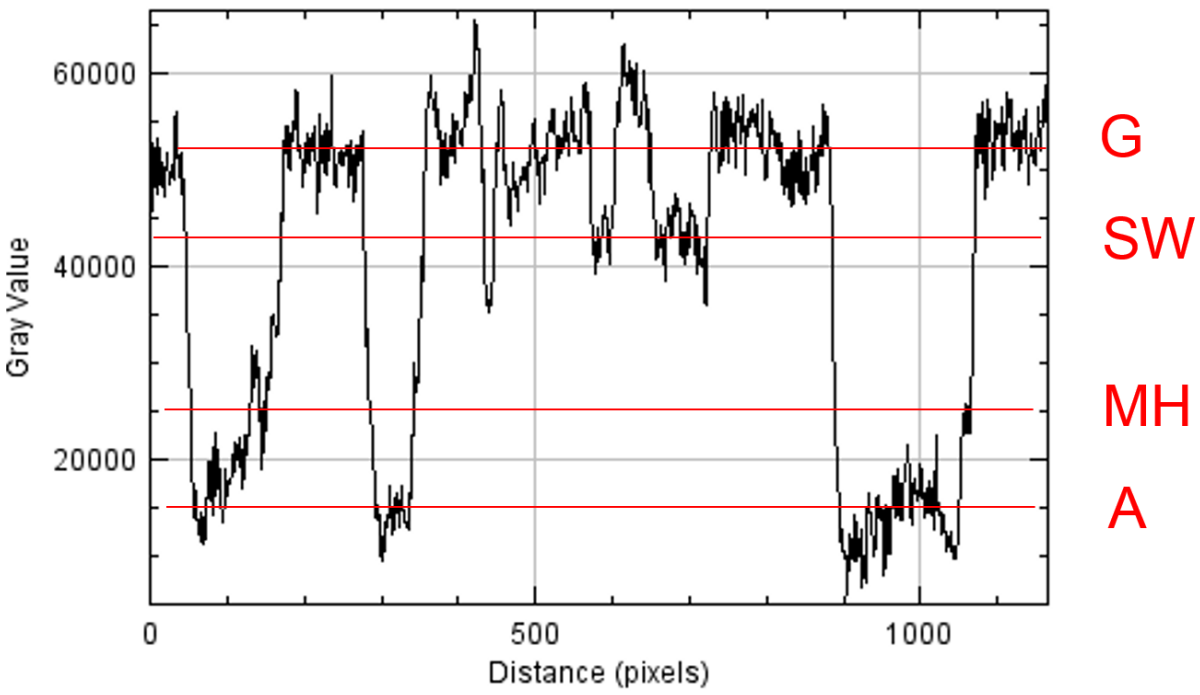

600

601 Figure 18. Gray level profile along yellow line in Figure 17.

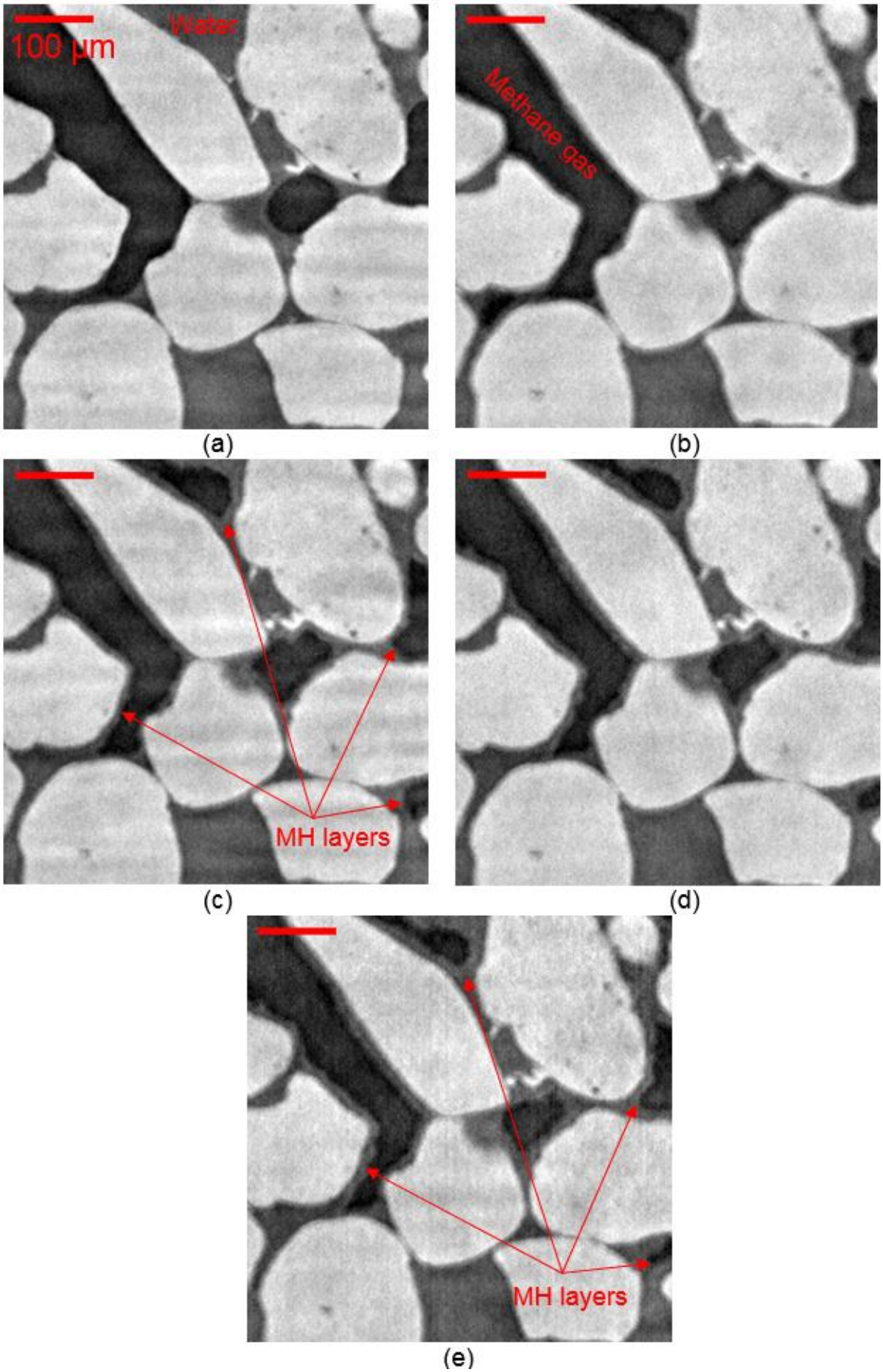

602

603 Figure 19. Vertical cross-section showing the MH formation (tap water) at: (a) t = 0.3

604 h; (b) t = 0.8 h; (c) t = 2.2 h; (d) t = 4.3 h; (e) t = 6.0 h.

605

References

Alavoine, A., Dangla, P., Pereira, and J.M. 2020. “Fast Fourier transform-based homogenisation of gas hydrate bearing sediments”. *Géotechnique Letters*, 10, 367-376.

Boswell, R., Moridis, G., Reagan, M., Berkeley, L., and Collett, T. S. 2011. “Gas hydrate accumulation types and their application to numerical simulation”. In Proceedings of the 7th International Conference on Gas Hydrates (p. 12).

Chand, S., Minshull, T. A., Gei, D., and Carcione, J. M. 2004. “Elastic velocity models for gas-hydrate-bearing sediments - A comparison”. *Geophysical Journal International*, 159(2), 573–590. https://doi.org/10.1111/j.1365-246X.2004.02387.x

Chaouachi, M., Falenty, A., Sell, K., Enzmann, F., Kersten, M., Haberth, D., and Werner, F. K. 2015. “Microstructural evolution of gas hydrates in sedimentary matrices observed with synchrotron X-ray computed tomographic microscopy”. *Geochemistry, Geophysics, Geosystems*, 16, 1711–1722. https://doi.org/10.1002/2015GC005811

Chen, X., and Espinoza, D. N. 2018. “Ostwald ripening changes the pore habit and spatial variability of clathrate hydrate”. *Fuel*, 214, 614–622. https://doi.org/10.1016/j.fuel.2017.11.065

Clayton, C. R. I., Priest, J. A., and Best, A. I. 2005. “The effects of disseminated methane hydrate on the dynamic stiffness and damping of a sand”. *Géotechnique*, 55(6), 423–434. https://doi.org/10.1680/geot.2005.55.6.423

Collett, T. S., Johnson, A. H., Knapp, C. C., and Boswell, R. 2009. “Natural gas hydrates: A review”. *The American Association of Petroleum Geologists*, 89, 146–219. https://doi.org/10.1306/13201101M891602

Dai, S., Santamarina, J. C., Waite, W. F., and Kneafsey, T. J. 2012. “Hydrate morphology: Physical properties of sands with patchy hydrate saturation”. *Journal of Geophysical Research B: Solid Earth*, 117(11). https://doi.org/10.1029/2012JB009667

Dvorkin, J., and Lavoie, D. 1999. Elasticity of marine sediments: “Rock physics modeling”. *Geophysical Research Letters*, 26(12), 1781–1784. https://doi.org/http://dx.doi.org/10.1029/1999GL900332

Dvorkin, J., and Nur, A. 1996. “Elasticity of high-porosity sandstones: Theory for two North Sea data sets”. *Geophysics*, 61(5), 890–893. https://doi.org/10.1190/1.1444059

Dvorkin, J., Helgerud, M. B., Waite, W. F., Kirby, S. H., and Nur, A. 2000. “Introduction to Physical Properties and Elasticity Models: Chapter 20”. https://doi.org/10.1007/978-94-011-4387-5_20

643 Helgerud, M. B., Dvorkin, J., and Nur, A. 1999. “Elastic-wave velocity in marine
644 sediments with gas hy-drates: Effective medium modeling”. *Geophysical Research*
645 *Letters*, 26(13), 2021–2024. https://doi.org/http://dx.doi.org/10.1029/1999GL900421

646 Kerkar, P., Jones, K. W., Kleinberg, R., Lindquist, W. B., Tomov, S., Feng, H., and
647 Mahajan, D. 2009. “Direct observations of three dimensional growth of hydrates
648 hosted in porous media”. *Applied Physics Letters*, 95(2), 2007–2010.
649 https://doi.org/10.1063/1.3120544

650 Kerkar, P. B., Horvat, K., Jones, K. W., and Mahajan, D. 2014. “Imaging methane
651 hydrates growth dynamics in porous media using synchrotron X-ray computed
652 tomography”. *Geochemistry Geophysics Geosystems*, 15, 4759–4768.
653 https://doi.org/10.1002/2014GC005373

654 King, A., Guignot, N., Zerbino, P., Boulard, E., Desjardins, K., Bordessoule, M.,
655 Leclerq, N., Le, S., Renaud, G., Cerato, M., Bornert, M., Lenoir, N., Delzon, S.,
656 Perrillat, J.-P., Legodec, Y., and Itié, J.-P. 2016 “Tomography and imaging at the
657 PSICHE beam line of the SOLEIL synchrotron,” *Review of Scientific Instruments*,
658 87(9).

659 Le, T. X., Aimedieu, P., Bornert, M., Chabot, B., Rodts, S., and Tang, A. M. 2019.
660 “Effect of temperature cycle on mechanical properties of methane hydrate-bearing
661 sediment”. *Soils and Foundations*, 59(4), 814-827.
662 https://doi.org/10.1016/j.sandf.2019.02.008

663 Le, T. X., Rodts, S., Hautemayou, D., Aimedieu, P., Bornert, M., Chabot, B., and
664 Tang, A. M. 2020. “Kinetics of methane hydrate formation and dissociation in sand
665 sediment”. Geomechanics for Energy and the Environment, 100103.
666 https://doi.org/10.1016/j.gete.2018.09.007

667 Le, T.X. 2019. “Experimental study on the mechanical properties and the
668 microstructure of methane-hydrate bearing sandy sediments”. PhD Thesis of
669 Université Paris-Est.

670 Lei, L., Seol, Y., and Jarvis, K. 2018. “Pore-Scale Visualization of Methane Hydrate-
671 Bearing Sediments With Micro-CT”. *Geophysical Research Letters*, 45(11), 5417–
672 5426. https://doi.org/10.1029/2018GL078507

673 Lei, L., Seol, Y., Choi, J. H., and Kneafsey, T. J. 2019. “Pore habit of methane
674 hydrate and its evolution in sediment matrix–Laboratory visualization with phase-
675 contrast micro-CT”. *Marine and Petroleum Geology*, 104, 451-467.

676 Nguyen-Sy, T., Tang, A.M., To, Q.D., and Vu, M.N. 2019. “A model to predict the
677 elastic properties of gas hydrate-bearing sediments”. *Journal of Applied Geophysics*,
678 169, 154 – 164. https://doi.org/10.1016/j.jappgeo.2019.05.003.

679 NIST XCOM: https://physics.nist.gov/PhysRefData/Xcom/html/xcom1.html

680 Paganin, D., Mayo, S. C., Gureyev, T. E., Miller, P. R., and Wilkins, S. W. 2002.
681 “Simultaneous phase and amplitude extraction from a single defocused image of a
682 homogeneous object”. *Journal of microscopy*, 206(1), 33-40.

683 Priest, J. A., Rees, E. V. L., and Clayton, C. R. I. 2009. “Influence of gas hydrate
684 morphology on the seismic velocities of sands”. *Journal of Geophysical Research:*
685 *Solid Earth*, 114(11). https://doi.org/10.1029/2009JB006284

686 Sloan, E. D. and Koh, C.A. 2008. “Clathrate Hydrates of Natural Gases”.

687 Swinehart, D. F. 1962. “The Beer-Lambert Law”. Journal of Chemical Education,
688 39(7), 333. https://doi.org/10.1021/ed039p333

689 Ta, X. H., Yun, T. S., Muhunthan, B., and Kwon, T. 2015. “Observations of pore-scale
690 growth patterns of carbon dioxide hydrate using X-ray computed microtomography”.
691 *Geochemistry Geophysics Geosystems*, 912–924.
692 https://doi.org/10.1002/2014GC005675

693 Taleb, F., Garziglia, S., and Sultan, N., 2018. “Hydromechanical Properties of Gas
694 Hydrate-Bearing Fine Sediments From In Situ Testing”. *Journal of Geophysical*
695 *Research: Solid Earth*, 123(11), 9615-9634.

696 Taleb, F., Lemaire, M., Garziglia, S., Marsset, T., and Sultan, N., 2020. “Seafloor
697 depressions on the Nigerian margin: Seabed morphology and sub-seabed hydrate
698 distribution”. *Marine and Petroleum Geology* 114, 104175.

699 Waite, W., Winters, W. J., and Mason, D. H. 2004. “Methane hydrate formation in
700 partially water-saturated Ottawa sand”. *American Mineralogist*, 89, 1202–1207.

701 Yang, L., Zhao, J., Liu, W., Li, Y., Yang, M., and Song, Y. 2015. “Microstructure
702 Observations of Natural Gas Hydrate Occurrence in Porous Media Using Microfocus
703 X-ray Computed Tomography”. *Energy & Fuels*, 29(8), 4835–4841.
704 https://doi.org/10.1021/acs.energyfuels.5b00881

705 Zhao, J., Yang, L., Liu, Y., and Song, Y. 2015. “Microstructural characteristics of
706 natural gas hydrates hosted in various sand sediments”. *Royal Society of Chemistry*,
707 17(35), 22632–22641. https://doi.org/10.1039/c5cp03698d

708